INORGANIC CHEMISTRY FRONTIERS

RESEARCH ARTICLE

View Article Online
View Journal | View Issue

Cite this: *Inorg. Chem. Front.*, 2025, **12**, 5430

Deep-ultraviolet nonlinear-optical crystals $LiBePO_4$ and BeP_2O_6 synthesized by ionic potential modulation towards uniform arrangement of PO_4 groups†

Xia Zhang,[a] Jian-Qiang Shen,[a] Hong-Xiao Lv,[b] Peng-Hui Guo,[a] Yi-Gang Chen, *[a] Chun-Li Hu*[c] and Xian-Ming Zhang *[a,b]

Received 17th March 2025,
Accepted 24th April 2025

DOI: 10.1039/d5qi00779h

rsc.li/frontiers-inorganic

The uniform arrangement of functional groups is a key factor in improving nonlinear properties in nonlinear-optical (NLO) materials, but currently there is no feasible and guiding strategy to modulate the uniform arrangement. Herein, we first apply the ionic potential concept to deep-ultraviolet (DUV, λ < 200 nm) NLO phosphates for a uniform arrangement of PO_4 tetrahedral functional groups. Adopting $Cs_4LiBe_4P_7O_{24}$ with a non-uniform arrangement of PO_4 as a structural model, by removing low ionic potential Cs^+ and Li^+ successively, two DUV NLO crystals $LiBePO_4$ and BeP_2O_6 were synthesized. $LiBePO_4$ features a $[Be_3P_3O_{18}]$ six-membered ring constructed by alternate connection of BeO_4 and PO_4, while BeP_2O_6 exhibits two kinds of $[PO_3]_\infty$ helical chains bridged by BeO_4. Remarkably, the arrangement of the PO_4 in $LiBePO_4$ and BeP_2O_6 exhibits uniform evolution. As a result, $LiBePO_4$ exhibits an enhanced second-harmonic-generation (SHG) effect up to 4.3 times that of $Cs_4LiBe_4P_7O_{24}$, while BeP_2O_6 shows an even more enhanced SHG effect, reaching 7.0 that of $Cs_4LiBe_4P_7O_{24}$ (2.1 × KDP). Moreover, BeP_2O_6 exhibits a short DUV absorption edge below 175 nm and the shortest SHG phase-matching output wavelength down to 211 nm. The universality of the new ionic potential modulation strategy is supported through analyzing known NLO materials containing alkali/alkaline-earth metal cations.

Introduction

The exploration of deep-ultraviolet (DUV, λ < 200 nm or band-gap > 6.2 eV) nonlinear-optical (NLO) crystals with large second-harmonic-generation (SHG) effects is of tremendous academic interest,[1,2] as a large SHG effect is beneficial for high laser frequency-conversion efficiency, which can be widely applied in a series of optoelectronic fields, *e.g.*, material micromachining, generation of entangled photon pairs, photo-electron spectroscopy, *etc.*[3–6] In particular, those crystals with both a large SHG effect and short SHG phase-matching output wavelength (preferably in the short-wave UV ($\lambda \leq 266$ nm), and even DUV region) are popular research areas because of essential applications in frontier technology. However, a large SHG effect and wide band-gap are naturally incompatible due to the fact that the SHG effect is inversely proportional to the band-gap in principle. Over the past few decades, a common strategy for achieving a large SHG effect has been to introduce SHG-active π-conjugated groups such as $[BO_3]$ and $[CO_3]$ to construct DUV NLO crystals, and this strategy has produced many crystals, such as $KBe_2BO_3F_2$ (KBBF),[7] $NH_4Be_2BO_3F_2$,[8] β-$Rb_2Al_2B_2O_7$,[9] $NH_4B_4O_6F$,[10] and $LiZn(OH)CO_3$.[11]

Recent studies show that non-π-conjugated tetrahedral groups such as $[SiO_4]$, $[PO_4]$, and $[SO_4]$ with large HOMO–LUMO gaps can achieve high transmittance in the DUV region, and a series of tetrahedral DUV NLO crystals were thus synthesized, *e.g.* Li_2SrSiO_4,[12] $Rb_6Si_{10}O_{23}$,[13] $Ba_3P_3O_{10}Cl$,[14] $Cs_6Mg_6(PO_3)_{18}$,[15] $RbNaMgP_2O_7$,[16] $Ba_5P_6O_{20}$,[17] $(NH_4)_2Na_3Li_9(SO_4)_7$,[18] *etc.* However, most of these DUV NLO crystals exhibit a small SHG effect because the constituent tetrahedral groups show nearly nonpolar high symmetry and therefore exhibit weak SHG activity. In order to improve the

---

[a] *Key Laboratory of Magnetic Molecules and Magnetic Information Material of Ministry of Education, School of Chemistry and Material Science, Shanxi Normal University, Taiyuan 030031, China. E-mail: yg_chen80@sina.com, zhangxm@dns.sxnu.edu.cn*

[b] *College of Chemistry & Chemical Engineering, Key Laboratory of Interface Science and Engineering in Advanced Material, Ministry of Education, Taiyuan University of Technology, Taiyuan, Shanxi 030024, P. R. China*

[c] *State Key Laboratory of Structural Chemistry, Fujian Institute of Research on the Structure of Matter, Chinese Academy of Sciences, Fuzhou 350002, China. E-mail: clhu@fjirsm.ac.cn*

† Electronic supplementary information (ESI) available: Crystallographic data, XPS spectra, powder XRD, TG and DSC curves, IR spectra. CCDC 2384142 and 2384141 for $LiBePO_4$ and BeP_2O_6. For ESI and crystallographic data in CIF or other electronic format see DOI: **https://doi.org/10.1039/d5qi00779h**

SHG performance, some strategies have been proposed, mainly including the introduction of (i) second-order Jahn–Teller effect d^0 cations (*e.g.* Mo^{6+}, Ti^{4+}) or ns^2 lone-pair cations (*e.g.* Pb^{2+}, Sn^{2+}),[19–22] (ii) anisotropic tetrahedral groups involving partially substituted oxygen atoms (*e.g.* $[BO_{4-x}F_x]$, $[PO_{4-x}F_x]$, $[SO_{4-x}(NH_2)_x]$),[23–26] and (iii) π-conjugated groups (*e.g.* $[BO_3]$).[27,28] However, the strategies all face seemingly insurmountable difficulties, such as an evident red-shift of the optical absorption edge, low thermal stability or returning to π-conjugated-characteristic NLO materials. Notably, that alkali/alkaline-earth metal cations with large HOMO–LUMO gaps have been only thought of as counterions for charge balance in these acentric structures, and their electrostatic interactions with surrounding tetrahedral groups are always overlooked. However, the interaction could affect the arrangement of tetrahedral groups, while a uniform arrangement can drive the generation of a large SHG effect according to anionic group theory.

In 2020, we reported two isostructural DUV NLO crystals $M_4LiBe_4P_7O_{24}$ (M = Cs, Rb) by combining alkali and alkaline-earth metal cations. Unfortunately, both crystals exhibit a weak SHG effect (~0.3 × KDP).[29] Structurally, the weak SHG effect is mainly caused by a non-uniform arrangement of PO_4 groups (Fig. S1†). Additionally, it is found that the characteristic differences between the three metal cations Cs^+, Li^+ and Be^{2+} in $Cs_4LiBe_4P_7O_{24}$ (as an example) are size and charge number. The influence of the size and charge number on the electrostatic interactions of the respective ions is consistent with the ionic potential concept. In this regard, we take $Cs_4LiBe_4P_7O_{24}$ as a structural model and put forward an ionic potential modulation strategy towards uniform arrangement of PO_4. By removing low ionic potential Cs^+ and Li^+, two NLO-active crystals $LiBePO_4$ and BeP_2O_6 were synthesized successively, and the arrangement of the PO_4 exhibits uniform evolution. An increased SHG effect from $Cs_4LiBe_4P_7O_{24}$ to $LiBePO_4$ to BeP_2O_6 is thus displayed. Notably, BeP_2O_6 exhibits a large SHG effect of 7.0 × $Cs_4LiBe_4P_7O_{24}$ (2.1 × KDP) and the shortest SHG phase-matching output down to the short-wave UV region of 211 nm. Furthermore, the universality of the ionic potential modulation strategy is supported through investigating known alkali/alkaline-earth metal NLO structures.

Experimental

Reagents

BeO (99.99%), $NH_4H_2PO_4$ (99.9%), Li_2CO_3 (99.99%), MoO_3 (99.9%) and Li_2MoO_4 (99.9%) were commercially available and used as received. Caution: due to the high toxicity of BeO upon inhalation, all experiments were performed with sufficient ventilation.

Synthesis

A polycrystalline sample of $LiBePO_4$ was synthesized by a solid-state reaction method. Stoichiometric amounts of Li_2CO_3, BeO, and $NH_4H_2PO_4$ were mixed, ground completely, put in a platinum crucible, and heated in a muffle furnace at 350 °C for 10 h. Then, the material was reground thoroughly, pressed into a pellet, and heated at 850 °C for 3d with several intermittent grindings.

Crystal growth

We used a high-temperature solution method to grow the crystals of $LiBePO_4$ and BeP_2O_6. For $LiBePO_4$, a mixture of $LiBePO_4$ polycrystalline powder (0.5 mmol, 0.055 g), MoO_3 (4 mmol, 0.576 g), and Li_2MoO_4 (3 mmol, 0.522 g) was melted at 850 °C, then quickly cooled to 750 °C and held for 10 h. Then, the melt was cooled to 550 °C at a rate of 3 °C h^{-1} and finally cooled to 350 °C at a rate of 20 °C h^{-1}, and we switched off the furnace. Colorless millimeter-crystals were obtained after dissolving the material in water.

For BeP_2O_6, a mixture of Li_2CO_3 (0.5 mmol, 0.037 g), BeO (1 mmol, 0.025 g) and $NH_4H_2PO_4$ (3 mmol, 0.345 g) was melted at 850 °C and held for 12 h. Then, the melt was cooled down to 400 °C at a rate of 1 °C h^{-1}. Finally, the melt was cooled down to 350 °C at a rate of 10 °C h^{-1}, and we switched off the furnace. Colorless millimeter-crystals were obtained after dissolving the material in water.

Single-crystal X-ray diffraction (XRD)

Single-crystal XRD data for $LiBePO_4$ and BeP_2O_6 were collected at 293 K on a Bruker D8 Venture diffractometer equipped with a graphite monochromator using Mo K_α radiation (λ = 0.71073 Å). Empirical absorption correction using spherical harmonics was performed using the SCALE3 ABSPACK scaling algorithm. The structure was solved by direct methods with the program SHELXS and refined by the full-matrix least-squares program SHELXL.[30] The structure was carefully checked using the program PLATON and no higher symmetries were found.[31] The details of relevant crystallographic data are summarized in Table 1. The atomic coordinates and equi-

Table 1 Crystal data and structure refinements for $LiBePO_4$ and BeP_2O_6

Empirical formula	$LiBePO_4$	BeP_2O_6
Formula weight	221.84	166.95
Temperature/K	293(2) K	293(2) K
Crystal system	Monoclinic	Monoclinic
Space group	*Cc*	$P2_1$
a/Å	16.331(1)	7.084(2)
b/Å	9.151(1)	8.586(3)
c/Å	15.965(1)	14.092(7)
α/°	90	90
β/°	111.62(1)	94.06(3)
γ/°	90	90
Volume/Å^3	2218.34(9)	855.0(6)
Z	16	8
ρ_{calc}/g cm^{-3}	2.117	2.594
μ/mm^{-1}	0.788	0.953
F(000)	1728	656
Goodness-of-fit on F^2	1.03	1.036
R_1, wR_2 $[I \geq 2\,\sigma(I)]^a$	0.0261, 0.0674	0.0328, 0.0793
R_1, wR_2 (all data)^a	0.0316, 0.0717	0.0381, 0.0823
Flack parameter	0.02(3)	−0.01(5)

[a] $R_1 = \sum||F_o|-|F_c||/\sum|F_o|$, and $wR_2 = [w(F_o^2-F_c^2)^2/w(F_o^2)^2]^{1/2}$.

valent isotropic displacement parameters are listed in Table S1.† The selected bond distances and angles are shown in Table S2.†

Powder X-ray diffraction (XRD)

Powder XRD data of $LiBePO_4$ and BeP_2O_6 were collected using a Rigaku MiniFlex600 powder diffractometer equipped with Cu K_α radiation (λ = 1.5418 Å) in the 2θ angular range of 5–80° with a scan step width of 0.01° at 293 K. These experimental XRD patterns were in good agreement with the calculated patterns (Fig. S2 and S3†).

Element analysis

Element analysis was performed by using a PerkinElmer Optima 8000 DV inductively coupled plasma optical emission spectrometer (ICP-OES). Two crystal samples were dissolved in perchloric acid at the boiling point for 0.5 h. ICP-OES measurements give molar ratios of 1.08(Li) : 0.95(Be) : 1.00(P) for $LiBePO_4$ and 1.00(Be) : 2.11(P) for BeP_2O_6, which are consistent with their formulae.

X-ray photoelectron spectroscopy (XPS)

The chemical states and surface compositions of $LiBePO_4$ and BeP_2O_6 were analyzed by a Thermo Scientific K-Alpha$^+$ X-ray photoelectron spectrometer with a monochromatic Al K_α X-ray source (1486.6 eV) operating at 72 W (12 kV, 6 mA). All of the XPS spectra underwent background subtraction and were fitted using mixed Gaussian-Lorentzian peak shapes.

As seen in Fig. S4,† XPS spectra of $LiBePO_4$ and BeP_2O_6 demonstrate the presence of Li (for $LiBePO_4$), Be, P, and O (Fig. S4a and f†). For $LiBePO_4$, a peak is observed at 55.38 eV for Li 1s, ascribed to the Li(I) oxidation state (Fig. S4b†). The Be 1s XPS spectrum (Fig. S4c†) shows a peak at 113.50 eV, which is attributed to the Be(II) oxidation state. The peak at 133.46 eV (Fig. S4d†) corresponds to the P 2p binding energy for the +5 oxidation state. The O 1s XPS spectrum exhibits a peak at 531.54 eV (O^{2-}) (Fig. S4e†). For BeP_2O_6, the Be 1s XPS spectrum (Fig. S4g†) shows a peak at 114.20 eV, which is attributed to the Be(II) oxidation state. The peak at 133.56 eV (Fig. S4h†) corresponds to the P 2p binding energy for the +5 oxidation state. The O 1s XPS spectrum exhibits a peak at 531.74 eV (O^{2-}) (Fig. S4i†).

Thermal behavior

Thermogravimetry (TG) and differential scanning calorimetry (DSC) analysis of $LiBePO_4$ and BeP_2O_6 were carried out on a NETZSCH STA 449 F5 Jupiter simultaneous analysis system under flowing N_2. About 15 mg of polycrystalline samples of $LiBePO_4$ and BeP_2O_6 were separately placed in Pt crucibles, and heated from room temperature to 1300 °C (for $LiBePO_4$) or 1100 °C (for BeP_2O_6) at a rate of 10 °C min^{-1} under a flowing N_2 atmosphere.

TG and DSC curves of $LiBePO_4$ and BeP_2O_6 (Fig. S5†) show that weight losses in the TG curves were not obviously observed up to 1300 °C for $LiBePO_4$ and 1100 °C for BeP_2O_6. An endothermic peak at 1263 °C in the DSC curve for $LiBePO_4$ was detected, while the endothermic peak of BeP_2O_6 was not observed until 1068 °C, indicating the excellent thermostability. Further, polycrystalline samples of $LiBePO_4$ and BeP_2O_6 were separately calcined at 1300 °C and 1100 °C for 0.5 h under an air atmosphere. Powder XRD of the residues (Fig. S2 and S3†) suggests that $LiBePO_4$ samples before and after melting are consistent, showing that it is a congruently melting compound, while BeP_2O_6 samples before and after melting are inconsistent. According to the powder XRD pattern of the residue, BeP_2O_6 after melting is transformed into another known polymorph BeP_2O_6 and an unknown phase (Fig. S3b†), demonstrating that BeP_2O_6 is an incongruently melting compound.

Infrared (IR) spectroscopy

Fourier transform infrared (FTIR) spectra of $LiBePO_4$ and BeP_2O_6 were recorded from KBr pellets in the range 4000–400 cm^{-1} on a Nicolet Model 5DX spectrometer. As shown in Fig. S6,† the IR spectrum of $LiBePO_4$ indicates that the peak at 1055 cm^{-1} is attributed to the P–O asymmetric stretching vibration of PO_4. The peaks at 789, 715, and 611 cm^{-1} are attributed to the P–O symmetric stretching vibrations of PO_4. The peaks at 577 and 508 cm^{-1} are attributed to the P–O bending vibrations of PO_4. The IR spectrum of BeP_2O_6 indicates that the peaks at 1287, 1174, 1109, 1030, and 995 cm^{-1} are attributed to the P–O asymmetric stretching vibrations of PO_4. The peak at 735 cm^{-1} is attributed to the P–O symmetric stretching vibration of PO_4. The peaks at 518 and 438 cm^{-1} are attributed to the P–O bending vibrations of PO_4. The IR spectra further indicate the presence of P–O units of $LiBePO_4$ and BeP_2O_6.

SHG measurement

Powder SHG measurements of $LiBePO_4$ and BeP_2O_6 were performed by the Kurtz–Perry method at 298 K. The measurement was carried out using a Q-switched Nd:YAG solid-state laser at 1064 nm and 532 nm, and the intensity of the frequency-doubled output emitted from the samples was measured using a photomultiplier tube. Polycrystalline samples $LiBePO_4$ and BeP_2O_6 were sieved into a series of distinct size ranges: 20–40 μm, 40–60 μm, 60–80 μm, 80–120 μm, 120–150 μm, 150–200 μm, and 200–300 μm. Polycrystalline KH_2PO_4 (KDP) and β-BaB_2O_4 (BBO) with the same particle size ranges were used as references. The SHG signal intensity of the $LiBePO_4$/KDP and BeP_2O_6/KDP (or BBO) ratio was identified based on the same size (150–200 μm).

Optical transmission spectrum

Optical transmission spectra of $LiBePO_4$ and BeP_2O_6 were measured using a Shimadzu SolidSpec-3700 DUV spectrometer in the 175–800 nm region. Two polished single-crystals with sizes of 2.0 × 1.2 × 0.3 mm^3 for $LiBePO_4$ and 1.8 × 1.1 × 0.3 mm^3 for BeP_2O_6 were separately used to perform the measurements.

Birefringence measurement

Birefringences of $LiBePO_4$ and BeP_2O_6 were measured on a CNOPTEC cross-polarizing microscope BK-POLR with an LED light filter. The LED light source has an optical wavelength of 590 ± 3 nm. The birefringence was calculated by using the following equation: $R = d \times |N_e - N_0| = d \times \Delta n$, where R, d, and Δn represent the optical retardation, thickness of the crystal, and birefringence, respectively.

Interference colors of the selected $LiBePO_4$ and BeP_2O_6 single-crystal samples are second-order yellow and second-order green based on a Michel–Levy diagram, and complete extinction can be achieved (Fig. S7a and S7b†). The tested crystals have retardations (R) of 810 and 710 nm, with thicknesses (d) of 45.13 and 25.23 μm, respectively. Accordingly, the measured birefringences are 0.018 and 0.028 for $LiBePO_4$ and BeP_2O_6, respectively.

Bond-valence-sum (BVS) calculation

BVS calculations for $LiBePO_4$ and BeP_2O_6 were performed to further validate the structural model, and the bond valence sums were calculated using the formula $V_i = \sum S_{ij} = \sum \exp[(r_0 - r_{ij})/B]$, where S_{ij} is the bond valence associated with the bond length r_{ij}, and r_0 and B (usually 0.37) are empirically determined parameters.

Computational method

Single-crystal structural data of $LiBePO_4$ and BeP_2O_6 were used for the theoretical calculations. The electronic structures and optical properties were calculated using a plane-wave pseudopotential method within density functional theory (DFT) implemented in the total energy code CASTEP.[32,33] Generalized gradient approximation (GGA) Perdew–Burke–Ernzerhof (PBE) was used as the exchange and correlation functional.[34] The norm-conserving pseudopotential was applied to present the core–electron interactions.[35] Li $2s^1$, Be $2s^2$, O $2s^2$ $2p^4$, and p $3s^2$ $2p^3$ orbital electrons were considered as valence electrons. A cutoff energy of 850 eV determined the number of plane waves included in the basis sets. Monkhorst–Pack k-point sampling of 2 × 1 × 4 was used to perform the numerical integration of the Brillouin zone. During the optical property calculations, about 540 empty bands were set to ensure the convergence of SHG coefficients. Birefringence is calculated by subtracting the minimum refractive index from the maximum refractive index. The theoretical birefringences of $LiBePO_4$ and BeP_2O_6 are 0.016 and 0.024, respectively, at 590 nm, which are close to the experimental results. The calculations of second-order NLO susceptibilities were based on length-gauge formalism within the independent particle approximation.[36,37]

Results and discussion

Crystal structures

$LiBePO_4$ and BeP_2O_6 single-crystals were synthesized through high-temperature molten reactions, and both crystal structures were characterized by single-crystal XRD. $LiBePO_4$ crystallizes in acentric and polar monoclinic space group Cc (no. 9), and contains eight crystallographically independent Li atoms, eight Be atoms and eight PO_4 groups, all of which are localized on crystallographically general positions with site occupancies of 1. Basic tetrahedral BeO_4 and PO_4 show typical bond distances of 1.606(3)–1.645(3) Å for Be–O and 1.525(1)–1.542(1) Å for P–O bonds. The material features a $[Be_3P_3O_{18}]$ six-membered ring constructed by alternate connection of BeO_4 and PO_4. The six-membered rings are fused by shared oxygen to generate $[BePO_4]_\infty$ two-dimensional (2D) pseudo layers in the ac plane (Fig. 1a). The pseudo layers are interconnected through Be–O–P bonds to form a 3D structure with pores (Fig. 1b). It should be noted that c glide planes in the structure cause polarization cancellation along the b-axis and net polarization in the ac plane. Small four-coordinated Li^+ fills in pores to balance charge (Fig. 1b). In comparison, in $Cs_4LiBe_4P_7O_{24}$, large high-coordinated Cs^+ requires large coordination space that induces four-coordinated Li^+ on large $[LiBe_4P_7O_{24}]$ twelve-membered rings of framework layers (Fig. S1†).

BeP_2O_6 crystallizes in acentric and polar monoclinic space group $P2_1$ (no. 4). There are four crystallographically independent Be atoms and eight PO_4 groups, all of which are localized on crystallographically general positions with Wyckoff letter $2a$. These PO_4 by corner-sharing generate two kinds of $[PO_3]_\infty$ helical chains with a 2_1 axis along the b-axis (Fig. 1c). Adjacent $[PO_3]_\infty$ chains are bridged by BeO_4 to produce a 3D structure. Net polarization of the structure is along the b-axis, as deduced from its $P2_1$ space group. Viewed along the b-axis (Fig. 1d), two $[PO_3]_\infty$ chains both exhibit almost uniform stacking. In all BeO_4 and PO_4 unis, Be–O (1.579(6)–1.633(6) Å) and P–O (1.434(4)–1.603(3) Å) bond lengths both vary in reasonable ranges. Validity of both structure models is checked through BVS calculations and XPS measurements, revealing their con-

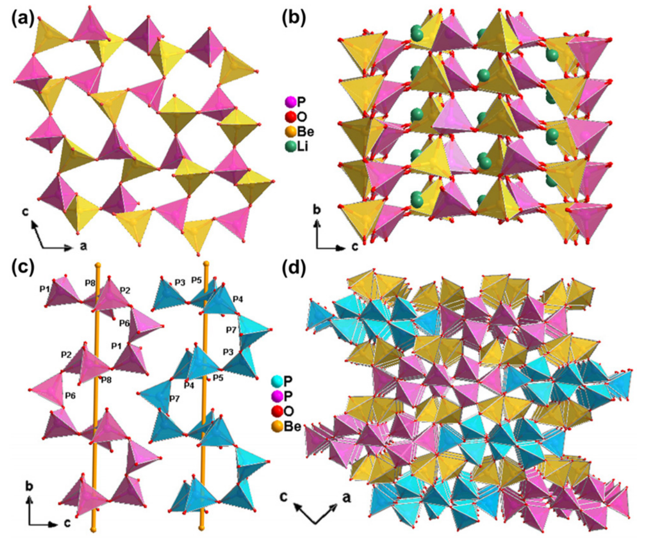

Fig. 1 Crystal structures of $LiBePO_4$ and BeP_2O_6. $LiBePO_4$: (a) $[BePO_4]_\infty$ 2D pseudo layer formed by $[Be_3P_3O_{18}]$ six-membered rings. (b) 3D stacking of $[BePO_4]_\infty$ pseudo layers viewed along the a-axis. BeP_2O_6: (c) two kinds of $[PO_3]_\infty$ chains with 2_1 helices along the b-axis. (d) 3D stacking of $[PO_3]_\infty$ chains bridged by BeO_4 viewed along the b-axis.

stituent elements in rational oxide states (Table S1 and Fig. S4†).

Ionic potential modulation model of PO_4 arrangement

Arrangement changes of the PO_4 from $Cs_4LiBe_4P_7O_{24}$ to $LiBePO_4$ to BeP_2O_6 are related to the respective counter-balance cations Cs^+, Li^+ and Be^{2+}. The Pauling electronegativity of these elements increases in turn from Cs (0.79) to Li (0.98) to Be (1.57). In $Cs_4LiBe_4P_7O_{24}$, Cs^+ has the strongest ionic bonding character and thus is regarded as the counter-balance cation of the structure, and the remaining ions Li^+ and Be^{2+} mainly act as local charge balancing cations in the structure. Similarly, in $LiBePO_4$, Li^+ is counter-balance cation of the structure and Be^{2+} mainly acts as a local charge balancing cation. The size and charge number are the main differences between these cations. Their effect on PO_4 arrangement is studied using an ionic potential modulation model. According to the equation $\varphi = z/r$ (φ, ionic potential; z, ionic charge number; r, ionic radius), z values of Cs^+, Li^+ and Be^{2+} are 1, 1 and 2, respectively, and r values (effective ionic radii) of these cations in $Cs_4LiBe_4P_7O_{24}$, $LiBePO_4$ and BeP_2O_6 are 0.18, 0.059 and 0.027 nm, respectively. φ_{Li^+} and $\varphi_{Be^{2+}}$ are calculated to be 16.95 and 74.07, 3.1 and 13.4 times greater, respectively, than 5.52 for φ_{Cs^+}. The impacts of the alkali/alkaline-earth metal cations on the respective PO_4 groups are depicted in the radar maps in Fig. 2. As shown in Fig. 2, with increasing φ from φ_{Cs^+} to φ_{Li^+} to $\varphi_{Be^{2+}}$, the arrangement of these PO_4 groups around the cations exhibits uniform evolution. The uniform evolution can bring the following advantages: (i) the number of PO_4 groups per unit volume increases, which is confirmed by calculating the packing density (ρ) of PO_4, showing that $\rho_{[PO4]}$ increases from 1.2×10^{-2} to 1.5×10^{-2} to 1.9×10^{-2} per $Å^3$; (ii) favorable superposition of microscopic hyperpolarizability of PO_4 that is beneficial for increasing the overall SHG effect is generated, and it is verified by calculating the dipole moment (μ) of PO_4, revealing that $\mu_{[PO4]}$ increases from 0, 0.7×10^{-3} to 4.5×10^{-3} Debye (D) $Å^{-3}$. Essentially, ionic potential modulation is mainly due to electrostatic interactions between alkali/alkaline-earth metal cations and surrounding ions. The electrostatic interaction can be estimated using Coulomb's law based on a simple point-charge model, revealing that the electrostatic interactions between Li^+ and P^{5+} in $LiBePO_4$ and between Be^{2+} and P^{5+} in BeP_2O_6 are 1.8 and 3.7 times that between Cs^+ and P^{5+} in $Cs_4LiBe_4P_7O_{24}$ (average distances of Cs and P, Li and P, and Be and P are 3.99, 3.00 and 2.93 Å according to Fig. 2). In addition, within the same structure, the ionic potential concept remains effective and applicable. In $Cs_4LiBe_4P_7O_{24}$ and $LiBePO_4$, the arrangement uniformity of the PO_4 surrounding $Cs^+/Li^+/Be^{2+}$ and Li^+/Be^{2+} is improved in turn (Fig. S8 and S9†).

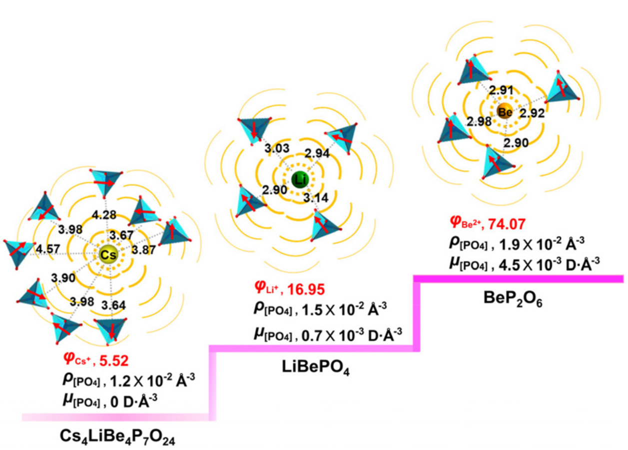

Fig. 2 Ionic potential (φ) modulation model of PO_4 arrangement. In the radar maps, the numbers and arrows represent the distance (Å) between the cations and dipole moment direction of PO_4. Only PO_4 tetrahedra are displayed for clarity.

SHG effect analysis

SHG effects based on the Kurtz–Perry method were measured at laser wavelengths 1064 and 532 nm, showing that the SHG effect of $LiBePO_4$ is 1.3 × benchmark KDP (KH_2PO_4) at 1064 nm (Fig. 3a), and 4.3 times that of $Cs_4LiBe_4P_7O_{24}$. The SHG effect of BeP_2O_6 further increases to 2.1 × KDP (Fig. 3a), reaching 7.0 times that of $Cs_4LiBe_4P_7O_{24}$, and meanwhile, BeP_2O_6 exhibits an SHG effect of 0.4 × BBO (β-BaB_2O_4) at 532 nm (Fig. 3c). The large SHG effect of BeP_2O_6 is compared not only with reported non-π-conjugated tetrahedral DUV NLO materials, such as $Ba_2NaClP_2O_7$ (0.9 × KDP),[38] $KMg(H_2O)PO_4$ (1.14 × KDP),[39] BPO_4 (2.0 × KDP),[40] Li_2SrSiO_4 (0.3 × KDP),[13] Li_3AlSiO_5 (0.8 × KDP),[41] $Li_2NaNH_4(SO_4)_2$ (1.1 × KDP),[18] and $LiKSO_4$ (1.2× KDP),[42] but also with well-known π-conjugated NLO materials, such as KBBF (1.21 × KDP),[7] LiB_3O_5 (LBO, 3.0 × KDP),[43] CsB_3O_5 (CBO, 2.7 × KDP),[44] and $CsLiB_6O_{10}$ (CLBO, 2.2 × KDP).[45] Furthermore, $LiBePO_4$ reveals phase-matchable behavior in the visible region, whereas BeP_2O_6 exhibits phase-matchable behavior in both visible and ultraviolet (UV) regions, as shown by the increasing SHG intensities with increasing particle size (Fig. 3b and d).

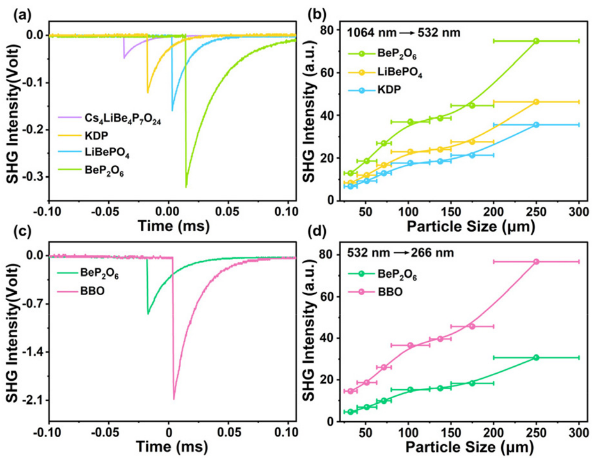

Fig. 3 (a) SHG signals and (b) SHG signal intensity *vs.* particle size for $LiBePO_4$, BeP_2O_6, and benchmarks $Cs_4LiBe_4P_7O_{24}$ and KDP at 1064 nm. (c) SHG signals and (d) SHG signal intensity *vs.* particle size for BeP_2O_6 and benchmark BBO at 532 nm.

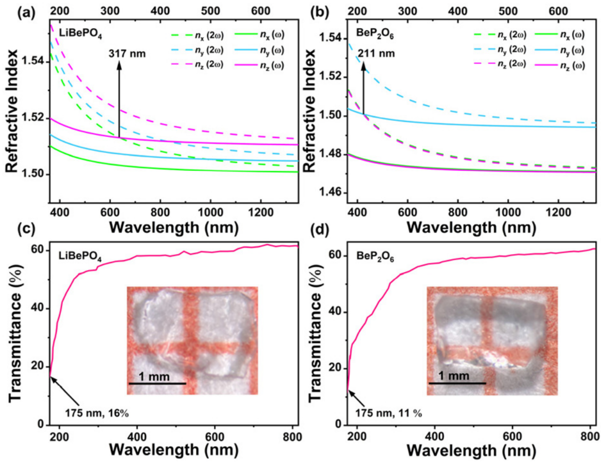

Fig. 4 Refractive index dispersions of (a) $LiBePO_4$ and (b) BeP_2O_6. Single-crystal transmission spectra of (c) $LiBePO_4$ and (d) BeP_2O_6, with single-crystal photographs in the insets.

The phase-matching capacities of both structures are studied through experimental and theoretical methods. Calculated refractive index dispersions (Fig. 4a and b) reveal that the shortest SHG phase-matching output wavelengths are 317 and 211 nm for $LiBePO_4$ and BeP_2O_6, respectively, consistent with the corresponding experimental observations of phase-matching in the 1064-to-532 nm and 532-to-266 nm second-harmonic processes (Fig. 3b and d), confirming their phase-matching capacity. In addition, calculated birefringences of $LiBePO_4$ and BeP_2O_6 are 0.016 and 0.024, respectively, at 590 nm, and experimental birefringences determined using a cross-polarizing microscope at 590 ± 3 nm through an optical retardation method show that the tested birefringences are 0.018 for $LiBePO_4$ and 0.028 for BeP_2O_6 (Fig. S7†), in general agreement with the calculated results. Remarkably, the shortest SHG phase-matching output of BeP_2O_6 is down to the short-wave UV region of 211 nm, much better than non-phase-matching BPO_4, 450 nm of $LiCs_2PO_4$,[46] and well-known borates LBO (277 nm), CBO (273 nm) and CLBO (236 nm) (Table 2). BeP_2O_6 may be applied to frequency quadruple and quintuple the Nd:YAG laser output, producing 266 nm and 213 nm coherent light. In addition, optical transmission spectra show that $LiBePO_4$ and BeP_2O_6 both have short DUV absorption edges below 175 nm (Fig. 4c and d), comparable to that of $Cs_4LiBe_4P_7O_{24}$ (<190 nm).[29]

Table 2 Comparison of DUV absorption edges (λ_{DUV}), SHG effects at 1064 nm, and SHG phase-matching cutoff wavelengths (λ_{PM}) of well-known crystals

Material	λ_{DUV} (nm)	SHG effect (×KDP)	λ_{PM} (nm)
BPO_4	134	2.0	Nonphase-matching
$LiCs_2PO_4$	174	2.6	450
LBO	158	3.0	277
CBO	167	2.7	273
CLBO	180	2.2	236
BeP_2O_6	**<175**	**2.1**	**211**

Theoretical calculation

To gain deep insight into the origin of the good optical properties of $LiBePO_4$ and BeP_2O_6, first-principles calculations were implemented. Band structures calculated using the hybrid exchange–correlation functional of HSE06 (Fig. 5a and c) indicate that $LiBePO_4$ and BeP_2O_6 have very wide band-gaps of 8.33 and 8.20 eV, corresponding to DUV absorption edges of 149 and 151 nm, respectively, in good support of the experimental results. Partial densities of states (Fig. 5b and d) show that the upper part of the valence-band consists mainly of P 3p, O 2p, and Be 2p electronic states, and the bottom part of the conduction-band is mainly composed of unoccupied P 3s 3p, O 2p, Be 2s 2p, and Li 2s (for $LiBePO_4$) orbitals, revealing that all the chemical bonding interactions (including P–O, Be–O and Li–O) make contributions to the optical transitions of $LiBePO_4$ and BeP_2O_6.

Calculated SHG coefficients show that the maximum tensors d_{15} for $LiBePO_4$ and d_{23} for BeP_2O_6 are 0.42 and 0.57 pm V^{-1}, respectively, close to experimentally measured SHG effects. To intuitively determine the main SHG-contributed electronic orbitals, SHG-density analyses for both maximum SHG tensors were carried out. For $LiBePO_4$ and BeP_2O_6, in the valence-band (Fig. 6a and c), the dominant SHG-contributed orbitals are O 2p nonbonding states, while in the conduction-band (Fig. 6b and d), unoccupied P 3s 3p and O 2p orbitals have a crucial impact on SHG effects, while the unoccupied Be 2p orbitals make a small contribution to the SHG effects. Furthermore, SHG contributions of different groups are summed based on the SHG-density analysis results shown in Fig. 6e, showing that PO_4 is in both cases the leading group

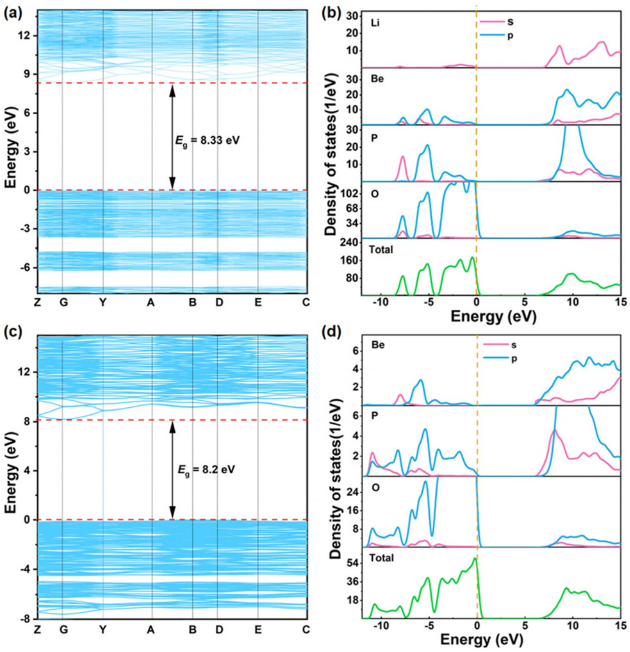

Fig. 5 Electronic band structures of (a) $LiBePO_4$ and (c) BeP_2O_6. Density of states diagrams for (b) $LiBePO_4$ and (d) BeP_2O_6.

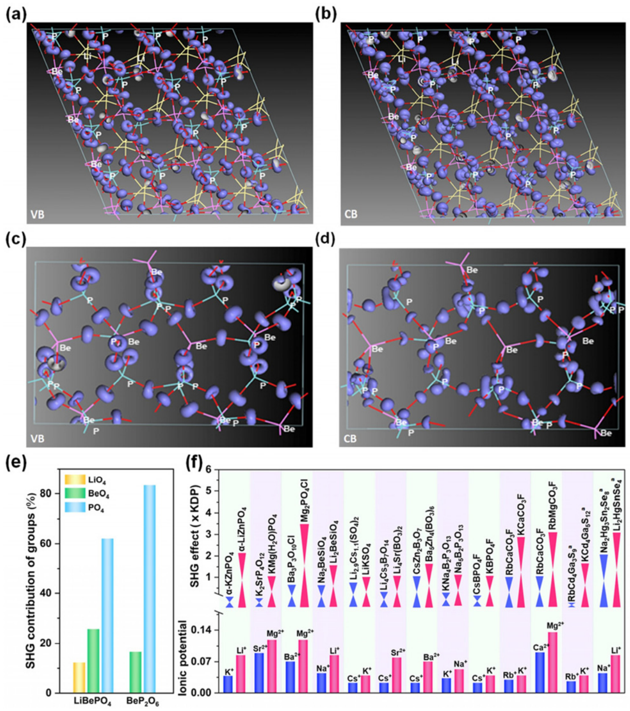

Fig. 6 SHG density maps of the valence band (VB) and conduction band (CB) for (a and b) $LiBePO_4$ and (c and d) BeP_2O_6. (e) SHG contribution of different groups in $LiBePO_4$ and BeP_2O_6. (f) Applicability of the ionic potential modulation strategy in known alkali/alkaline-earth metal NLO materials. Blue represents cations with low ionic potential and their corresponding compounds, and red represents cations with high ionic potential and their corresponding compounds. ^{a} Represents the SHG effect based on benchmark AGS ($AgGaS_2$).

producing SHG effects, accounting for 62.1% in $LiBePO_4$ and 83.4% in BeP_2O_6. The BeO_4 groups make small contributions to the SHG effects, accounting for 25.6% in $LiBePO_4$ and 16.6% in BeP_2O_6, respectively. The applicability of the ionic potential modulation strategy is investigated for known NLO structures containing alkali/alkaline-earth metal cations (Fig. 6f and Table S3†), and it is found that the strategy can be applied to these NLO materials well.

Conclusions

An ionic potential modulation strategy is applied to tetrahedral DUV NLO phosphates that have long suffered from a weak SHG effect. Taking $Cs_4LiBe_4P_7O_{24}$ as a structural prototype, through continuous removal of low ionic potential Cs^+ and Li^+, two DUV NLO crystals $LiBePO_4$ and BeP_2O_6 were successfully synthesized. $LiBePO_4$ exhibits a 3D structure constructed from $[Be_3P_3O_{18}]$ six-membered rings composed of alternate BeO_4 and PO_4, while BeP_2O_6 features a 3D structure constructed from two kinds of $[PO_3]_\infty$ helical chains bridged by BeO_4. Notably, the arrangement of PO_4 in $LiBePO_4$ and BeP_2O_6 exhibits uniform evolution. Thus, an increased SHG effect from $Cs_4LiBe_4P_7O_{24}$ to $LiBePO_4$ to BeP_2O_6 is generated. Furthermore, BeP_2O_6 exhibits a large SHG effect of 7.0 × $Cs_4LiBe_4P_7O_{24}$ (2.1 × KDP), the shortest SHG phase-matching output down to the short-wave UV region of 211 nm, and a short DUV absorption edge below 175 nm, showing that BeP_2O_6 is a potential short-wave UV NLO crystal. Moreover, the new modulation strategy is universally supported through known alkali/alkaline-earth metal NLO materials. This work may not only be used to update the possible roles of alkali/alkaline-earth metal cations in NLO materials but also provide new opportunities for the precise design of material structures and properties.

Author contributions

All authors have given approval to the final version of the manuscript.

Data availability

The detailed crystallographic information and ESI figures and tables can be found in the ESI.† Crystallographic data are available *via* the Cambridge Crystallographic Data Centre (CCDC): 2384142 and 2384141 for $LiBePO_4$ and BeP_2O_6. The data supporting this article have been included as part of the ESI.†

Conflicts of interest

There are no conflicts to declare.

Acknowledgements

This work was supported by the NSFC (21971155, 5207021329), Fundamental Research Program of Shanxi Province (202303021221153).

References

1 E. Goulielmakis, M. Schultze, M. Hofstetter, V. S. Yakovlev, J. Gagnon, M. Uiberacker, A. L. Aquila, E. Gullikson, D. T. Attwood and R. Kienberger, Single-cycle nonlinear optics, *Science*, 2008, **320**, 1614–1617.
2 P. S. Halasyamani and J. M. Rondinelli, The must-have and nice-to-have experimental and computational requirements for functional frequency doubling deep-UV crystals, *Nat. Commun.*, 2018, **9**, 2972.
3 C. Wu, X. X. Jiang, Y. L. Hu, C. B. Jiang, T. H. Wu, Z. S. Lin, Z. P. Huang, M. G. Humphrey and C. Zhang, A lanthanum ammonium sulfate double salt with a strong SHG response and wide deep–UV transparency, *Angew. Chem.*, 2022, **134**, e202115855.
4 J. X. Zhang, Q. G. Yue, S. H. Zhou, X. T. Wu, H. Lin and Q. L. Zhu, Screening strategy identifies an overlooked

deep–ultraviolet transparent nonlinear optical crystal, *Angew. Chem., Int. Ed.*, 2024, **63**, e202413276.

5 Z.-S. Feng, Z.-H. Kang, F.-G. Wu, J.-Y. Gao, Y. Jiang, H.-Z. Zhang, Y. M. Andreev, G. V. Lanskii, V. V. Atuchin and T. A. Gavrilova, SHG in doped GaSe: In crystals, *Opt. Express*, 2008, **16**, 9978–9985.

6 B. M. Oxley, J. B. Cho, A. K. Iyer, M. J. Waters, J. He, N. C. Smith, C. Wolverton, V. Gopalan, J. M. Rondinelli and J. I. Jang, Heteroanionic control of exemplary second-harmonic generation and phase matchability in 1D $LiAsS_{2-x}Se_x$, *J. Am. Chem. Soc.*, 2022, **144**, 13903–13912.

7 C. T. Chen, Y. B. Wang, Y. N. Xia, B. C. Wu, D. Y. Tang, K. Wu, Z. Wenrong, L. H. Yu and L. F. Mei, New development of nonlinear optical crystals for the ultraviolet region with molecular engineering approach, *J. Appl. Phys.*, 1995, **77**, 2268–2272.

8 G. Peng, N. Ye, Z. S. Lin, L. Kang, S. L. Pan, M. Zhang, C. S. Lin, X. F. Long, M. Luo and Y. Chen, $NH_4Be_2BO_3F_2$ and γ–Be_2BO_3F: Overcoming the layering habit in $KBe_2BO_3F_2$ for the next–generation deep–ultraviolet nonlinear optical materials, *Angew. Chem.*, 2018, **130**, 9106–9110.

9 T. T. Tran, N. Z. Koocher, J. M. Rondinelli and P. S. Halasyamani, Beryllium–free β–$Rb_2Al_2B_2O_7$ as a possible deep–ultraviolet nonlinear optical material replacement for $KBe_2BO_3F_2$, *Angew. Chem., Int. Ed.*, 2017, **129**, 3015–3019.

10 G. Q. Shi, Y. Wang, F. F. Zhang, B. B. Zhang, Z. H. Yang, X. L. Hou, S. L. Pan and K. R. Poeppelmeier, Finding the next deep-ultraviolet nonlinear optical material: $NH_4B_4O_6F$, *J. Am. Chem. Soc.*, 2017, **139**, 10645–10648.

11 X. M. Liu, L. Kang, P. F. Gong and Z. S. Lin, $LiZn(OH)CO_3$: A deep–ultraviolet nonlinear optical hydroxycarbonate designed from a diamond–like structure, *Angew. Chem., Int. Ed.*, 2021, **60**, 13574–13578.

12 H. P. Wu, B. B. Zhang, H. W. Yu, Z. G. Hu, J. Y. Wang, Y. C. Wu and P. S. Halasyamani, Designing silicates as deep–UV nonlinear optical (NLO) materials using edge–sharing tetrahedra, *Angew. Chem.*, 2020, **132**, 9007–9011.

13 S. Z. Huang, Y. Yang, J. B. Chen, W. Q. Jin, S. C. Cheng, Z. H. Yang and S. L. Pan, "Removing center"–An effective structure design strategy for nonlinear optical crystals, *Chem. Mater.*, 2022, **34**, 2429–2438.

14 P. Yu, L.-M. Wu, L.-J. Zhou and L. Chen, Deep-ultraviolet nonlinear optical crystals: $Ba_3P_3O_{10}X$ (X = Cl, Br), *J. Am. Chem. Soc.*, 2014, **136**, 480–487.

15 Y.-G. Chen, M.-L. Xing, P.-F. Liu, Y. Guo, N. Yang and X.-M. Zhang, Two phosphates: Noncentrosymmetric $Cs_6Mg_6(PO_3)_{18}$ and centrosymmetric $Cs_2MgZn_2(P_2O_7)_2$, *Inorg. Chem.*, 2017, **56**, 845–851.

16 S. G. Zhao, X. Y. Yang, Y. Yang, X. J. Kuang, F. Q. Lu, P. Shan, Z. H. Sun, Z. S. Lin, M. C. Hong and J. H. Luo, Non-centrosymmetric $RbNaMgP_2O_7$ with unprecedented thermo-induced enhancement of second harmonic generation, *J. Am. Chem. Soc.*, 2018, **140**, 1592–1595.

17 S. G. Zhao, P. F. Gong, S. Y. Luo, L. Bai, Z. S. Lin, Y. Y. Tang, Y. L. Zhou, M. C. Hong and J. H. Luo, Tailored synthesis of a nonlinear optical phosphate with a short absorption edge, *Angew. Chem., Int. Ed.*, 2015, **54**, 4217–4221.

18 T. Baiheti, S. J. Han, A. Tudi, Z. H. Yang and S. L. Pan, Alignment of polar moieties leading to strong second harmonic response in $KCsMoP_2O_9$, *Chem. Mater.*, 2020, **32**, 3297–3303.

19 Y. Q. Li, F. Liang, S. G. Zhao, L. N. Li, Z. Y. Wu, Q. R. Ding, S. Liu, Z. S. Lin, M. C. Hong and J. H. Luo, Two non-π-conjugated deep-UV nonlinear optical sulfates, *J. Am. Chem. Soc.*, 2019, **141**, 3833–3837.

20 T.-L. Chao, W.-J. Chang, S.-H. Wen, Y.-Q. Lin, B.-C. Chang and K.-H. Lii, Titanosilicates with strong phase-matched second harmonic generation responses, *J. Am. Chem. Soc.*, 2016, **138**, 9061–9064.

21 Y. Y. Yang, Y. Xiao, B. X. Li, Y.-G. Chen, P. H. Guo, B. B. Zhang and X.-M. Zhang, Stereochemically active lone-pair containing metal substitution in polar axis toward a giant phase-matchable optical nonlinear silicate crystal $Li_3(OH)PbSiO_4$, *J. Am. Chem. Soc.*, 2023, **145**, 22577–22583.

22 S. J. Han, A. Tudi, W. B. Zhang, X. L. Hou, Z. H. Yang and S. L. Pan, Recent development of SnII, SbIII–based birefringent material: Crystal chemistry and investigation of birefringence, *Angew. Chem., Int. Ed.*, 2023, **62**, e202302025.

23 M. Mutailipu and S. L. Pan, Emergent deep–ultraviolet nonlinear optical candidates, *Angew. Chem., Int. Ed.*, 2020, **59**, 20302–20317.

24 C.-Y. Pan, X.-R. Yang, L. Xiong, Z.-W. Lu, B.-Y. Zhen, X. Sui, X.-B. Deng, L. Chen and L.-M. Wu, Solid-state nonlinear optical switch with the widest switching temperature range owing to its continuously tunable T_c, *J. Am. Chem. Soc.*, 2020, **142**, 6423–6431.

25 H. Tian, N. Ye and M. Luo, Sulfamide: A Promising deep–ultraviolet nonlinear optical crystal assembled from polar covalent $[SO_2(NH_2)_2]$ tetrahedra, *Angew. Chem., Int. Ed.*, 2022, **61**, e202200395.

26 X. F. Wang, X. Leng, Y. Kuk, J. Lee, Q. Jing and K. M. Ok, Deep–ultraviolet transparent mixed metal sulfamates with enhanced nonlinear optical properties and birefringence, *Angew. Chem.*, 2024, **136**, e202315434.

27 Z. Y. Zhou, Y. Qiu, F. Liang, L. S. Palatinus, M. Poupon, T. Yang, R. H. Cong, Z. S. Lin and J. L. Sun, $CsSiB_3O_7$: A beryllium-free deep-ultraviolet nonlinear optical material discovered by the combination of electron diffraction and first-principles calculations, *Chem. Mater.*, 2018, **30**, 2203–2207.

28 H. N. Liu, H. P. Wu, Z. G. Hu, J. Y. Wang, Y. C. Wu and H. W. Yu, $Cs_3[(BOP)_2(B_3O_7)_3]$: A deep-ultraviolet nonlinear optical crystal designed by optimizing matching of cation and anion groups, *J. Am. Chem. Soc.*, 2023, **145**, 12691–12700.

29 Y.-G. Chen, C. Y. Yang, F. Wang, Y. Guo, X. X. Jiang and X.-M. Zhang, $M_4LiBe_4P_7O_{24}$ and $M_4Li(Li_3P)P_7O_{24}$ (M = Cs, Rb): Deep-ultraviolet nonlinear-optical phosphates with a

tetrahedra-substituted paracelsian-like framework, *Chem. Commun.*, 2020, **56**, 8639.

30 G. M. Sheldrick, A short history of SHELX, *Acta Crystallogr. Sect. A: Found. Crystallogr.*, 2008, **64**, 112–122.

31 A. L. Spek, Single-crystal structure validation with the program PLATON, *Acta Crystallogr. Sect. A: Found. Crystallogr.*, 2003, **36**, 7–13.

32 V. Milman, B. Winkler, J. A. White, C. J. Pickard, M. C. Payne, E. V. Akhmatskaya and R. H. Nobes, Electronic structure, properties, and phase stability of inorganic crystals: A pseudopotential plane-wave study, *Int. J. Quantum Chem.*, 2000, **77**, 895–910.

33 M. D. Segall, P. J. D. Lindan, M. J. Probert, C. J. Pickard, P. J. Hasnip, S. J. Clark and M. C. Payne, First-principles simulation: Ideas, illustrations and the CASTEP code, *J. Phys.: Condens. Matter*, 2002, **14**, 2717–2744.

34 J. P. Perdew, K. Burke and M. Ernzerhof, Generalized gradient approximation made simple, *Phys. Rev. Lett.*, 1996, **77**, 3865–3868.

35 J. S. Lin, A. Qteish, M. C. Payne and V. Heine, Optimized and transferable nonlocal separable *ab initio* pseudopoten tials, *Phys. Rev. B: Condens. Matter Mater. Phys.*, 1993, **47**, 4174–4180.

36 J. E. Sipe and E. Ghahramani, Nonlinear optical response of semiconductors in the independent-particle approxi mation, *Phys. Rev. B: Condens. Matter Mater. Phys.*, 1993, **48**, 11705–11722.

37 S. Sharma, J. K. Dewhurst and C. Ambrosch-Draxl, Linear and second-order optical response of III-V monolayer superlattices, *Phys. Rev. B: Condens. Matter Mater. Phys.*, 2003, **67**, 165332.

38 J. Chen, L. Xiong, L. Chen and L.-M. Wu, $Ba_2NaClP_2O_7$: Unprecedented phase matchability induced by symmetry breaking and its unique fresnoite-type structure, *J. Am. Chem. Soc.*, 2018, **140**, 14082–14086.

39 Z. Y. Bai, C.-L. Hu, L. H. Liu, L. Z. Zhang, Y. S. Huang, F. F. Yuan and Z. B. Lin, $KMg(H_2O)PO_4$: A deep-ultraviolet transparent nonlinear optical material derived from $KTiOPO_4$, *Chem. Mater.*, 2019, **31**, 9540–9545.

40 Z. H. Li, Z. S. Lin, Y. C. Wu, P. Z. Fu, Z. Z. Wang and C. T. Chen, Crystal growth, optical properties measurement, and theoretical calculation of BPO_4, *Chem. Mater.*, 2004, **16**, 2906–2908.

41 X. L. Chen, F. F. Zhang, L. L. Liu, B.-H. Lei, X. Y. Dong, Z. H. Yang, H. Y. Li and S. L. Pan, Li_3AlSiO_5: The first aluminosilicate as a potential deep-ultraviolet nonlinear optical crystal with the quaternary diamond-like structure, *Phys. Chem. Chem. Phys.*, 2015, **18**, 4362.

42 P. F. Zhu, P. F. Gong, Z. Y. Wang, H. T. Jiang, J. F. Zhao, C. Li, Z. S. Lin, X. L. Duan and F. P. Yu, Enlargement of bandgap and birefringence in nonlinear optical alkali-metal sulfate crystals by the substitution of asymmetrical non-π-conjugated cation, *Adv. Opt. Mater.*, 2023, **11**, 2301152.

43 C. T. Chen, Y. C. Wu, A. Jiang, B. Wu, G. You, R. Li and S. J. Lin, New nonlinear-optical crystal: LiB_3O_5, *J. Opt. Soc. Am.*, 1989, **6**, 616–621.

44 Y. C. Wu, T. Sasaki, S. Nakai, A. Yokotani, H. G. Tang and C. T. Chen, CsB_3O_5: A new nonlinear optical crystal, *Appl. Phys. Lett.*, 1993, **62**, 2614–2615.

45 J.-M. Tu and D. A. Keszler, $CsLiB_6O_{10}$: A noncentrosymmetric polyborate, *Mater. Res. Bull.*, 1995, **30**, 209–215.

46 L. Li, Y. Wang, B.-H. Lei, S. J. Han, Z. H. Yang, K. R. Poeppelmeier and S. L. Pan, A new deep-ultraviolet transparent orthophosphate $LiCs_2PO_4$ with large second harmonic generation response, *J. Am. Chem. Soc.*, 2016, **138**, 9101–9104.